



Research article

Differentiated strategy is a crucial approach to improve urban flood resilience



Mingyang Liu^a Ying Zhao^b, Xiangzhou Xu^{a,*} Hongwu Zhang^{c,**}

^a School of Infrastructure Engineering, Dalian University of Technology, Dalian, 116024, China

^b Water Resources Research Institute of Shandong Province, Shandong, Jinan, 250013, China

^c State Key Laboratory of Hydraulics and Hydrosystems, Tsinghua University, Beijing, 100084, China

ARTICLE INFO

Keywords:

Urban flood resilience
Flood intensity
System performance curve
Morphological characteristics
Resilience enhancement

ABSTRACT

The increasing frequency of extreme rainfall events in urban areas has highlighted the need for a focus on urban resilience to achieve effective emergency and mitigation planning. This study presents a multi-stage evaluation framework that integrates curve morphological feature parameters derived from urban flood intensity within grid cells, demonstrated through a case study in Shahekou District, Dalian City, China. The results show that morphological parameters, particularly the centroid indicator, provided an accurate description of resilience prioritization and performance differences. The two grids showed similar characteristics, but the centroid positions were 81.03 and 80.83 min in the middle stage and 313.07 and 307.53 min in the late stage, respectively. Increased rainfall intensity led to a reduction in flood resilience. The flood resilience values were 0.993, 0.992, 0.991, and 0.990, for return periods of 50, 100, 150, and 200 years, respectively. The interaction between the landscape pattern of the catchment area and intensity level of urban flooding creates distinct resilience mechanism. Two clusters with lower resilience exhibited significant retarding effects in the middle and late stages, which were negatively correlated with road density, with Pearson correlation coefficients of 0.41 and 0.57, respectively. These findings underscore the importance of developing differentiated resilience strategies tailored to specific resilience clusters, such as staged drainage interventions and landscape optimization.

1. Introduction

In recent years, extreme rainstorms that exceed existing drainage capacities have become increasingly frequent and problematic. Climate change is causing the hydrological cycle to accelerate as rising temperatures increase the rate of evaporation (WMO, 2020). Rainfall characterized by short duration and high intensity is more likely to cause flood disasters in urban areas with high runoff and low soil infiltration rates (Fan et al., 2024). Recent studies show that 1.81 billion people (23 % of the world population) are directly exposed to 1-in-100-year floods (McDermott, 2022). In East Asia, high-hazard settlements have expanded 60 % faster than flood-safe settlements, which will inevitably lead to increasing flood exposure (Rentschler et al., 2023). China, as a particularly vulnerable region, experiences varying degrees of urban flooding annually. For example, in 2019, rainfall in the urban area of Dalian reached 235.6 mm, causing direct economic losses of 890 million yuan. More recently, the Zhengzhou flood of 2021, caused by

unprecedented heavy rainfall, resulted in the deaths or disappearances of 380 people (Dong et al., 2022). Traditional approaches to urban flood risk management are no longer able to cope with evolving flood risks (Liu et al., 2024b). In recent years, disaster resilience has become one of the most widely investigated fields. The UN defined the concept of disaster resilience in one sentence: The ability of a system, community or society exposed to hazards to resist, absorb, accommodate to and recover from the effects of a hazard in a timely and efficient manner, including the preservation and restoration of its essential basic structures and functions (UNISDR, 2009). Urban flood resilience encompasses three stages of the flood cycle: preventive capacity in the early phase, coping capacity in the middle phase, and recovery and adaptation in the late phase (Liu et al., 2024a). This comprehensive approach incorporates the dynamic characteristics of flood disasters to facilitate risk mitigation. In summary, integrating resilience into urban flood management systems represents a critical and timely advancement to improve disaster preparedness, response, and recovery.

* Corresponding author.

** Corresponding author.

E-mail addresses: xzxu@dlut.edu.cn (X. Xu), zhhw@mail.tsinghua.edu.cn (H. Zhang).

Urban flood resilience assessment serves as a practical link between theoretical concepts and practical implementation. Methods such as indicator systems and system performance curves are commonly employed for assessment (Zou et al., 2024). This indicator-based method constructs resilience frameworks by selecting relevant metrics, enabling comparative analyses of flood resilience across cities or regions over time. It emphasizes the capacity to adapt to external shocks, engage across multiple dimensions, and learn in the aftermath of a disaster (Liu et al., 2024a). However, this method relies heavily on the selection of indicators, which may introduce subjectivity or result in a narrow evaluative perspective. Additionally, the approach struggles to capture the dynamic evolution of individual flood events, limiting its applicability in real-time disaster response scenarios. The system performance curve method, on the other hand, is used to show how system performance changes over time during a specific urban flood event (Fig. S1). The area enclosed by the performance curve and the time axis represents the engineering resilience of the system. The system performance reflects the representative functionality or characteristics of the whole system under the influence of flooding. Commonly used metrics in this field of research include inundation depth and land use (Chen et al., 2021), flood hazard metrics, such as water depth and flow rate (Zheng et al., 2024), the connectivity of road systems (Zhang et al., 2023a), as well as disaster losses and inundated areas (Zhang et al., 2023b). The performance curve method offers distinct advantages over the indicator-based approach. The former method employs hydrological and hydrodynamic modeling to minimize subjective bias and enhance scientific validity (Su et al., 2023). Furthermore, this approach provides a more accurate reflection of actual disaster dynamics in the real-time monitoring of urban system dynamics under extreme rainfall (Wang et al., 2019).

The characteristics of the system performance curve are distilled into a series of feature parameters corresponding to the early, middle, and late phases. The indicators provide a basis for exploring flood disaster response and emergency mechanisms across multiple stages. The shape of the curve is determined by the ability of each grid to contain its internal flooding, thereby enabling the derivation of diverse feature parameters (Qian et al., 2024; Simonovic and Peck, 2022). Current research has extensively examined parameters such as robustness, redundancy, flexibility, rapidity, resistance shape, and recovery degree (Haghbin and Mahjouri, 2023; Wu et al., 2022; Wang et al., 2024). However, existing methodologies exhibit several notable limitations. First, while these methods are effective in measuring total system resilience, the design does not sufficiently account for significant dynamic variations observed in trajectories. For example, two systems may have similar recovery times and variation rates. However, their trajectories could be entirely different: one might initially recover quickly but then slow down, while another may initially slowly recover but subsequently stabilize more rapidly (Abbasnejadfar et al., 2022). Such distinctions, which are crucial for optimizing emergency response and resource allocation strategies, remain indistinguishable through conventional urban flood frameworks. Second, current research lacks a comprehensive characterization of multi-stage flood resilience. This limitation hinders cross-stage comparability and prevents a holistic assessment of the entire disaster cycle (Cheng et al., 2021). Finally, geographical attributes, such as topography and land use within the catchment, have a profound impact on flood resilience (Shukla et al., 2025). While these factors are known to affect flood resilience, their specific effects on the characteristics of the curve remain insufficiently quantified. This knowledge gap significantly constrains the development of spatially tailored strategies.

This study uses numerical simulation to explore the evolution of urban flood resilience under multiple disaster scenarios. The objectives of this work are to (1) develop a multi-stage resilience assessment framework from a morphological perspective, (2) analyze the dynamic changes in urban flood resilience, (3) identify the resilience patterns associated with the characteristic parameters of each stage, and (4)

investigate the relationship among these patterns and urban landscape morphology. The analysis centers on Shahekou District in Dalian, China, seeking to understand the unequal nature of urban resilience.

2. Study area and related datasets

Located in the southernmost part of Northeast China ($120^{\circ}58' - 123^{\circ}31'E$, $38^{\circ}43' - 40^{\circ}10'N$), Dalian is the second-largest city in Liaoning Province. By the end of 2023, the population had exceeded 7 million, with a GDP of nearly 1 trillion yuan. The annual average rainfall is approximately 600 mm, with 60–70 % of the total occurring between June and September (Chen et al., 2022a). The period is often characterized by typhoons and heavy rainfall, which often leads to severe localized flooding.

Shahekou District, one of the central urban areas of Dalian with an area of 48.32 km^2 , was selected as the study region (Fig. 1). The district, located in the heart of Dalian, is the largest and most populous area of the city. The Malan River, which flows through the entire district from west to south and empties into the Yellow Sea, serves as the primary flood and drainage channel. In recent years, the expansion of impervious surfaces has heightened the susceptibility to urban flooding. Historical waterlogging incidents are concentrated around Funing Street, Wuyi Road, Zhongshan Road, and Malan River, where the altitude is lower and the buildings are relatively densely packed. Hence, the district provides a suitable case for investigating urban flood resilience.

Data on the underlying surface of the Shahekou District included elevation derived from a digital elevation model (DEM), as well as specifications of drainage networks, water systems, land use, building footprints, and road infrastructure. The DEM data, sourced from the European Space Agency, had a spatial resolution of 30 m (<https://spacedata.copernicus.eu/collections/copernicus-digital-elevation-model>). The drainage network data, provided by the Dalian City Construction Management Bureau, consists of 1552 manholes, 1793 conduits, and 24 outlets (Fig. S2a). The combined rain and sewage system, designed for a 1 to 5-year return period, represents a critical component of flood management. All vector data for building outlines, roads, and forests were obtained from Amap (<https://ditu.amap.com/>). Land use classification was derived from the Essential Urban Land Use Categories Map for China (<https://data-starcloudpcl.ac.cn/iearthdata/>) (Fig. S2b).

3. Methodology

As illustrated in Fig. 2, the research framework involves: (1) using InfoWorks ICM to simulate urban flooding and obtain the time-series data of flood depth and water velocity across each grid under different design rainfall scenarios; (2) inputting the data for both street and non-street locations into the flood intensity models to derive the system performance curve for each grid; (3) using the morphological characteristics parameters of the system performance curve to estimate urban flood resilience across various disaster scenarios; and (4) clustering the feature parameters to uncover the influence mechanism of urban morphological characteristics on urban flood resilience.

3.1. Rainfall events and urban flood modeling

Rainfall events were categorized into design rainfall and observed rainfall. The short-term heavy rainfall intensity was calculated using the revised formula from the Dalian Meteorological Service Center (Equation (1)) (Yuan, 2022). Rainstorms with different return periods (1, 2, 3, 50, 100, 150, and 200 years), a duration of 2 h, and a peak factor of 0.4 were selected as the designed rainstorm scenarios for this study. The measured rainfall was obtained from a tipping bucket rain gauge during a 2-h precipitation event on June 9, 2025 (Fig. 3a). The recorded rainfall amount reached 41.6 mm, which corresponds to a 2-h rainfall event with a return period of 1 year. Both design rainfall scenarios (with return periods of 1, 2, and 3 years) and measured rainfall were selected for

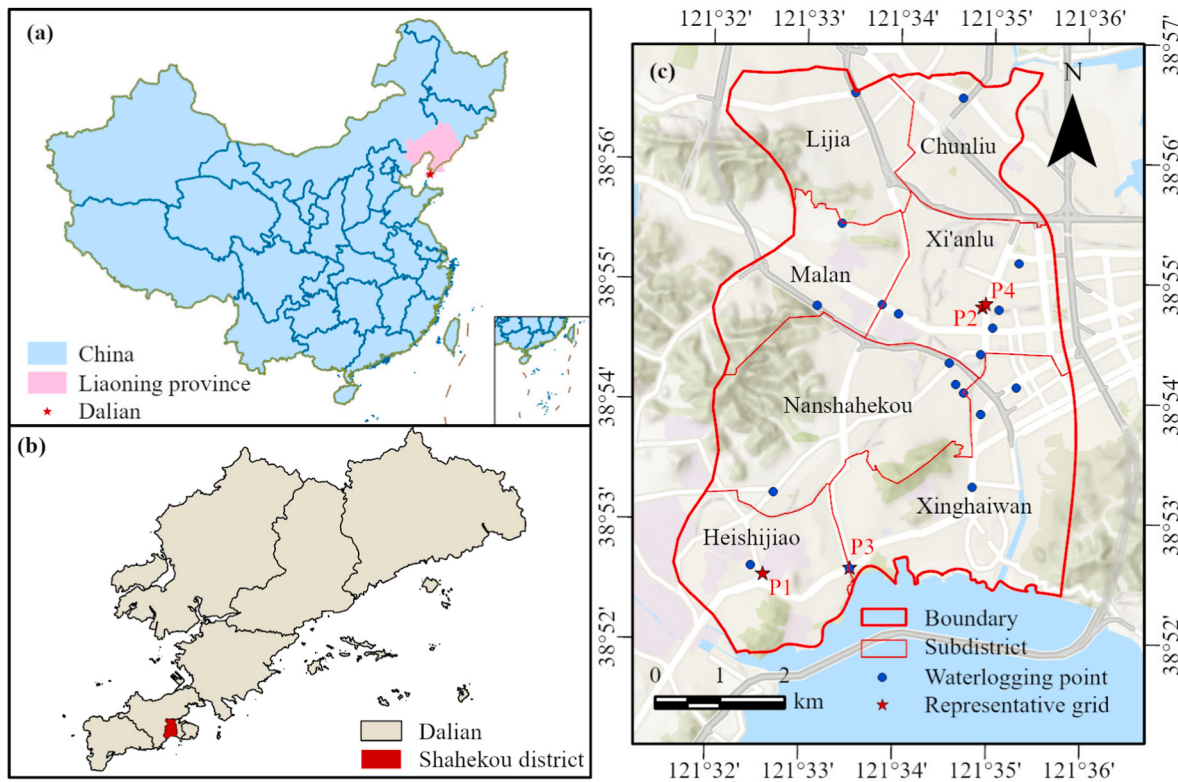


Fig. 1. Study area. Maps of (a) China, (b) Dalian City, and (c) Shahekou District. Shahekou District includes seven subdistricts: Chunliu, Heishijiao, Lijia, Malan, Nanshahekou, Xi'anlu, and Xinghaiwan.

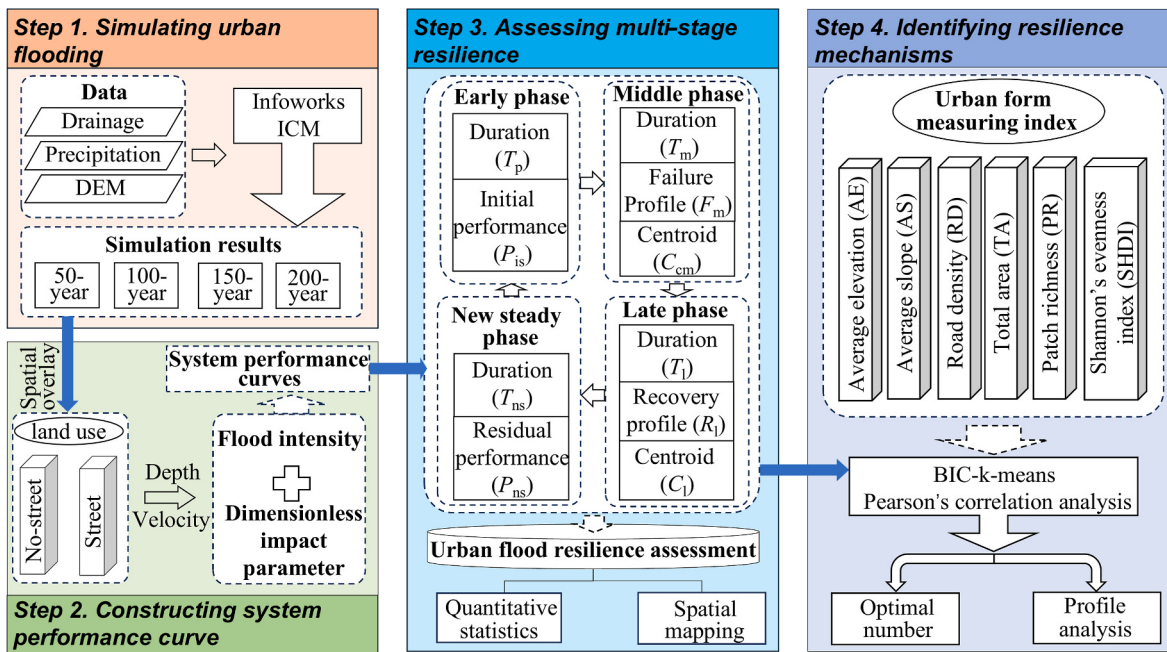


Fig. 2. Schematic diagram of the developed methodology.

model parameter calibration and validation purposes.

$$i = \frac{1261.362(1 + 0.659 \lg R)}{167(t + 7.508)^{0.63}} \quad (1)$$

where i refers to the rainfall intensity (mm/h), R is the rainfall return period (years), and t is the duration of a rainfall event (min).

The flood model established in this work was based on InfoWorks ICM. The model incorporated four main datasets: the existing drainage network, land use classifications, a DEM, and building outlines. The drainage network data provided information on manholes and conduits. Land use images were utilized to define the functions of the land surface and the distribution of forests. From June 19 to 20, 2025, a 20 % random sample of 533 land units was investigated in the field to verify the

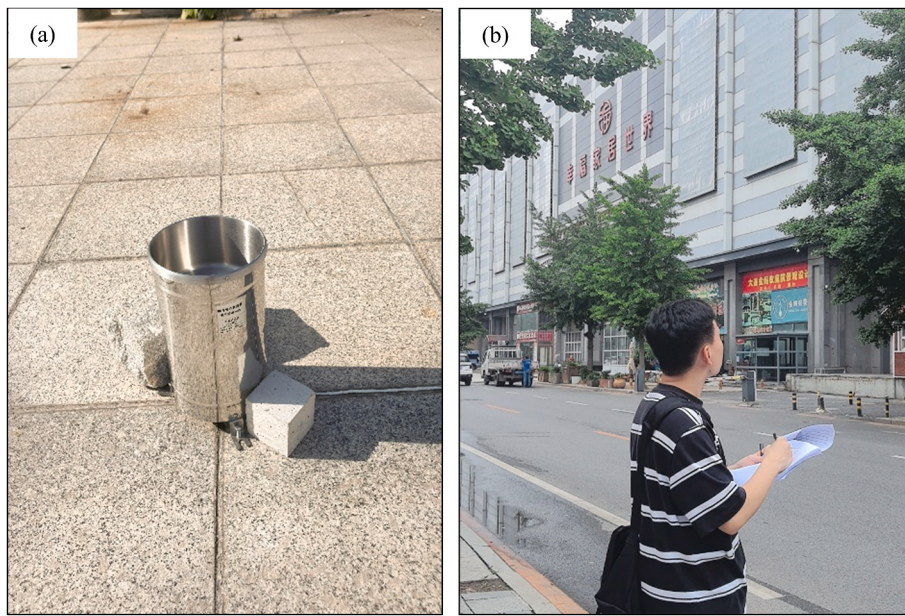


Fig. 3. High-precision data acquisition. (a) A tipping bucket rain gauge installed on April 12, 2025 (121.53°E, 38.79°N) for hydrological monitoring, and (b) field validation of land-use data accuracy through ground surveys conducted during June 19–20, 2025.

accuracy of the data (Fig. 3b). The catchments were delineated through spatial analysis of road networks, drainage systems, administrative boundaries, land use patterns, and topographic features. Each catchment was designed to discharge into manholes within its boundary. For catchments without available pipe network data, particularly in forested regions, surface runoff was drained into adjacent low-lying catchments. A total of 615,598 unstructured grid cells were used in the 2D model, with minimum and maximum areas of 25 m² and 100 m², respectively. In the context of the emergency response process, 3-h, 6-h, and 12-h time points are considered key operational milestones (Zhou et al., 2024). The total simulation time in the study was set to 720 min, accounting for both the rainfall duration and complexity calculations. Details regarding model establishment, calibration, and results are included in the [supplementary materials](#).

3.2. System performance indicator

Key feature parameters were extracted from system performance curves of each grid and used to calculate urban flood resilience. A distinction was made between street and non-street areas to account for the large spatial extent of the study area and the diversity of land use types. The system performance of the two categories was calculated separately to characterize the change. Python 3.8.5 was used as a coding language to develop models.

Urban flood intensity was treated as a representative indicator of the system. Hazards in non-street areas were quantified using the flood intensity method proposed by Vojtek and Vojteková (2016), as shown in Equation (2):

$$FI_{non-street}(i, t) = \begin{cases} 0 & d(i, t) = 0 \\ \frac{d(i, t)}{d(i, t) \cdot v(i, t)} & d(i, t) > 0 \text{ and } v(i, t) \leq 1 \\ v(i, t) & v(i, t) \geq 1 \end{cases} \quad (2)$$

where $FI_{non-street}(i, t)$ is the flood intensity of grid i at time t , $d(i, t)$ is the newly added flood depth of the grid i at time t (m), $v(i, t)$ is the flood velocity of grid i at time t (m/s). The specific classification of $FI_{non-street}(i, t)$ referred to Vojtek and Vojteková (2016): (0, 0.3] is the low intensity level, indicating that owners of land and buildings may be reminded of potential flood risks; (0.3, 1] is the medium intensity level, indicating the need for a detailed assessment of functions in the area and advising

against further expansion of the building footprint; (1, $+\infty$) is the high intensity level, necessitating flood prevention measures or the development of relocation plans to ensure adequate risk mitigation.

As outlined in the method proposed by Chen et al. (2021), the system performance for grids in non-street areas was computed using the upper and lower thresholds as shown in Equation (3).

$$P_{non-street}(i, t) = \begin{cases} 1 & FH_{non-street}(i, t) \leq 0.3 \\ \frac{1 - FH_{non-street}(i, t)}{1 - 0.3} & 0.3 < FH_{non-street}(i, t) \leq 1 \\ 0 & FH_{non-street}(i, t) > 1 \end{cases} \quad (3)$$

where $P_{non-street}(i, t)$ is the system performance of grid i at time t .

The heightened flood exposure of roadways motivated the selection of the physical model of human or vehicle stability in urban flood scenarios proposed by Lazzarin et al. (2022) to represent the flood intensity of grid cells in urban streets (Equations (4) and (5)).

$$W = \left(\frac{d}{Y_w} \right)^{\alpha} (1 + \beta Fr^2), Y_w > 0, \alpha \geq 1, \beta \geq 0 \quad (4)$$

$$Fr = v / \sqrt{gd} \quad (5)$$

where Y_w is a dimensionless parameter that is used as a reference depth to measure the actual water depth d (m). α and β are calibration factors that measure the relative importance of the static and dynamic components of W . g is gravity and Fr is the Froude number. The specific parameter values are listed in Lazzarin et al. (2022). A value of $W \leq 0.35$ indicates stability in flood, while a value exceeding it signifies instability.

Similarly, Equations (6) and (7) defined the system performance curve for the grid on the street.

$$P_{street}(i, t) = \begin{cases} 1 & W_{max}(i, t) \leq 0.35 \\ \frac{1 - W_{max}(i, t)}{1 - 0.35} & 0.35 < W_{max}(i, t) \leq 1 \\ 0 & W_{max}(i, t) > 1 \end{cases} \quad (6)$$

$$W_{max}(i, t) = \max [W_{residents}(i, t), W_{vehicles}(i, t)] \quad (7)$$

where $P_{street}(i,t)$ is the system performance of grid i on the street at time t . $W_{residents}(i,t)$ is the dimensionless impact parameter of people in grid i at time t . $W_{vehicles}(i,t)$ is the dimensionless impact parameter of vehicles in grid i at time t . $W_{max}(i,t)$ is the dimensionless impact parameter of grid i at time t .

3.3. Urban flood resilience assessment method

A resilience assessment method for urban flooding was developed by integrating various resilience indicators. Guided by existing research (Nan and Sansavini, 2017; Qian et al., 2024), this work defined ten feature parameters through four critical stages in the curve (Fig. 4). The parameters were then employed to assess flood resilience. Ayyub (2013) analyzes the system performance curve across the early, middle, and late stages to determine the degree of resilience. Accordingly, a centroid correction factor was introduced into the model to account for the trajectory of the curve during the middle and late stages. A new stability stage was incorporated to provide a more comprehensive and accurate representation of resilience (Equations (8)–(12)).

$$R(i) = \frac{T_p P_{is} + F_m T_m / t'_{cm} + R_l T_l / t_{cl} + P_{ns} T_{ns}}{T} \quad (8)$$

$$F_m = \frac{\int_{t_m}^{t_l} P(i,t) dt}{T_m} \quad (9)$$

$$R_l = \frac{\int_{t_l}^{t_{ns}} P(i,t) dt}{T_l} \quad (10)$$

$$t'_{cm} = \frac{\int_{t_m}^{t_l} t P(i,t) dt}{\int_{t_m}^{t_l} P(i,t) dt} + t_l \quad (11)$$

$$t_{cl} = \frac{\int_{t_l}^{t_{ns}} t P(i,t) dt}{\int_{t_l}^{t_{ns}} P(i,t) dt} \quad (12)$$

where $R(i)$ is the urban flood resilience of grid i . T_p , T_m , T_l , and T_{ns} are the durations of the early, middle, late, and new stable phases, respectively. P_{is} and P_{ns} are the system performance in the early and new stable phases. The horizontal coordinates t_{cm} and t_{cl} of the centroids C_m and C_l are used to describe the shape. To align the calculation results with the

concept of resilience, t'_{cm} is obtained by symmetrizing t_{cm} around $t = t_l$, so that as t'_{cm} and t_{cl} both decrease, resilience increases. T is the total simulation time of the model. Equations (13) and (14) describe the weighted average of the resilience capacities of different catchments and subdistricts.

$$R_{catchment}(j) = \frac{\sum_{i=1}^N (R(i) \cdot a(i))}{\sum_{i=1}^N a(i)} \quad (13)$$

$$R_{subdistrict}(k) = \frac{\sum_{i=1}^M (R(i) \cdot a(i))}{\sum_{i=1}^M a(i)} \quad (14)$$

where $R_{catchment}(j)$ is the urban flood resilience of catchment j . $R_{subdistrict}(k)$ is the urban flood resilience of subdistrict k . N is the total number of grids in catchment j . M is the total number of grids in subdistrict k . $a(i)$ is the area of grid i .

3.4. BIC-k-means clustering method

The purpose of the cluster analysis in the paper was to group catchments with similar characteristics and disaster response mechanisms, allowing for the development of targeted resilience strategies. The k-means algorithm was chosen for the analysis. Additionally, the Bayesian Information Criterion (BIC) method was used to determine the optimal number and quality of k-means clustering algorithms, thereby minimizing human subjectivity in selection. A detailed description of the calculation principles and procedures is provided in the [supplementary materials](#). The smaller the BIC score, the better the quality of the k-means clustering. The relationship between these clusters and the urban form characteristics of the catchments was examined to further explore resilience characteristics. Based on a survey of the existing literature and their identified research gaps (Liu et al., 2022; Mei et al., 2024; Zhang et al., 2020), six parameters were selected to describe the spatial characteristics of urban form: average elevation (AE), average slope (AS), road density (RD), total area (TA), patch richness (PR), and Shannon's evenness index (SHDI). Here, urban flood resilience was the dependent variable for each catchment, while the six urban form parameters acted

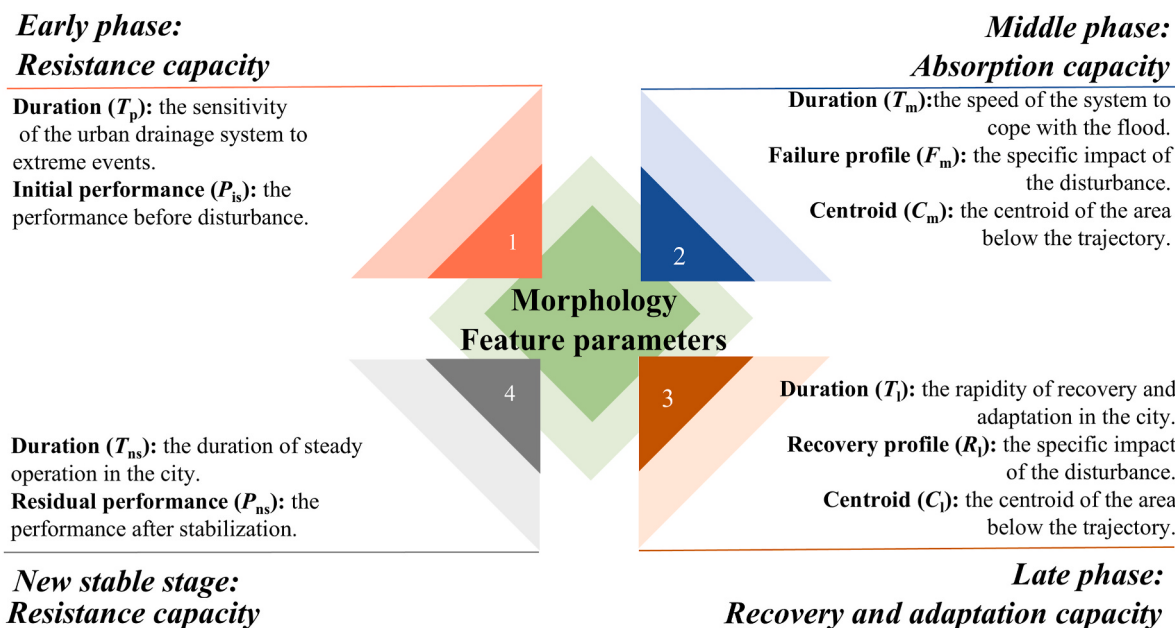


Fig. 4. Defining feature parameters from morphological changes of curves.

as the independent variables. Pearson's correlation analysis revealed the binary correlation between each factor and identified significant explanatory variables for urban flood resilience.

4. Results

4.1. Classification accuracy and system performance curve

The accuracy of flood simulations is inherently dependent on the reliability of urban land use data. A total of 107 units were randomly selected from the study area to ensure a representative description of the land use pattern. A confusion matrix was employed to calculate the producer's and user's coefficients, which were then used to determine the overall coefficient and Kappa coefficient (Debnath et al., 2023). As shown in Table 1, the overall coefficient and Kappa coefficient are 0.9 and 0.8, respectively. These metrics provide comprehensive measures of agreement between the classified image and the actual land cover distribution. A Kappa coefficient closer to 1 indicates a higher level of classification accuracy. Notably, residential areas were identified with high precision, with both producer's and user's coefficients exceeding 0.9. Land use categories, such as industrial areas and forests, achieved a coefficient of 1.0, which may reflect the limited availability of sampling data for these categories. In contrast, commercial service and business office categories showed a lower coefficient, highlighting greater challenges in automated classification for complex land uses. Overall, the methodology exhibited high accuracy and reliability in the Shahekou area, supporting its utility for subsequent flood simulation applications.

The system performance trends are similar across various grids. The system performance for grids showed a sharp decrease from 1 to a minimum value and recovered to 1, which was consistent with previous research (Chen et al., 2021; Wang et al., 2019; Zheng and Huang, 2023). The actual trajectory of system performance varies very significantly due to the unique properties of each grid. Changes in the system performance are divided into three types: full recovery to the initial level, recovery to a level below the initial, and a minimum point of 0. Fig. 5 illustrates four representative grids, carefully selected from both street and non-street areas, which exemplify the three typical performance curves. Grid P1, geographically situated in front of Walmart on Shuma Road in the Heishijiao Subdistrict, was categorized as building land. Grid P2 was also classified as building land near Wusi Square in the Xi'anlu Subdistrict. Grid P3, located at the intersection of Zhongshan Road and Xinan Road in the Xinghai Subdistrict, fell under traffic land,

while Grid P4, adjacent to Wusi Square in the Xi'anlu Subdistrict, was likewise categorized as traffic land. As shown in Fig. 5, during a 200-year return period of heavy rainfall, the durations of different stages showed significant variations between P1 and P3. For P1, the early, middle, late, and new steady stages lasted 60, 65, 300, and 295 min, respectively. In contrast, P3 exhibited durations of 65, 20, 55, and 580 min for each stage. While P1 and P3 reached the maximum performance score of 1, P2 and P4 did not meet this level. This occurs primarily because the two grids are located near historical waterlogging points, resulting in a performance that consistently remains below 1. The findings also indicate that the range of changes in the system performance increases with the return period of rainfall. The variation in system performance is most pronounced in Fig. 5c, where the minimum system performance reached 0 under a 200-year return period rainfall event. The primary reason is that urban roads, especially those in low-lying areas with steep gradients, are prone to rapid flooding during intense rainfall. The combined effects of water depth and flow velocity exacerbate instability for pedestrians and vehicles on roads compared to other land use types.

The proposed method also highlights the importance of the centroids in the middle and late stages as key features of the curve. Fig. 6 shows the characteristic parameters of the resilience indicators for P1 during rainfall events with return periods of 150 and 200 years. The F_m and R_l values for P1 were approximately 0.50 and 0.55, respectively, during the two rainfall events. If evaluated using traditional methods, both curves would ultimately exhibit the same resilience. However, the observed downward and upward trajectories differed significantly (Fig. 5a). The positions of the centroids (C_m and C_l) were 80.83 and 81.01 min for one curve, while 307.53 and 313.07 min for the other, respectively. Four grids were selected as representative cases to illustrate the diverse hydrological response patterns observed across different land use types.

4.2. Urban flood resilience

Flood resilience decreases with an increase in design rainfall intensity, but different subdistricts exhibit varying characteristics. The average flood resilience values of the area across four design rainfall scenarios with the return periods of 50, 100, 150, and 200 years were 0.993, 0.992, 0.991, and 0.990, respectively. Fig. S3a shows the changing pattern of flood resilience across the seven subdistricts of Shahekou District under the four design rainfall scenarios. Specifically, Lijia Subdistrict and Nanshahekou Subdistrict exhibited the highest resilience, with mean values of 0.997 and 0.995, respectively. The resilience of Lijia Subdistrict was primarily attributed to its topographic position at higher elevations. Nanshahekou Subdistrict has the largest forest cover among the seven subdistricts, which accounts for 45 % of the total urban forest ecosystem. Urban forests help reduce urban stormwater flows, thereby contributing to higher flood resilience. The results were generally consistent with previous research (Chen et al., 2021). Fig. S3b illustrates the average flood resilience at each stage across various subdistricts for a design rainfall with a return period of 200 years. The maximum resilience values in the early, middle, late, and new steady phases occurred in the Lijia, Lijia, Lijia, and Xi'anlu Subdistricts, respectively. In contrast, the minimum resilience values occurred in Xi'anlu, Xi'anlu, Xi'anlu, and Heishijiao Subdistricts. Notably, during the middle and late stages, the flood resilience in each subdistrict was approximately 0.24, indicating similar characteristics across subdistricts across these stages.

The spatial distribution of urban flood resilience remains relatively consistent across different designed rainfall intensities. Fig. 7 shows the resilience values in the Shahekou District under design rainfalls with return periods of 50, 100, 150, and 200 years. Under a design rainfall with a return period of 50 years, the categories of very low and low catchments were mainly located in the lower altitudes of Nanshahekou, Xi'anlu, Chunliu, and Xinghaiwan Subdistricts, with 4, 3, 2, and 1, respectively. In contrast, all catchments in the Lijia Subdistrict were of

Table 1
Accuracy assessment of the classified land use maps.

Categories	Quantity	Sampling	Producer's coefficient	User's coefficient
Industrial area	7	4	1.0	1.0
Park	35	4	0.7	1.0
Educational zone	57	9	0.8	1.0
Residential area	302	65	0.9	0.9
Forest	6	2	1.0	1.0
Business area	36	7	1.0	0.6
Commercial service zone	57	11	0.8	0.6
Cultural and sports area	11	2	1.0	1.0
Administrative zone	10	1	1.0	1.0
Medical zone	12	2	1.0	1.0
Overall coefficient			0.9	
Kappa coefficient			0.8	

Notes: Producer's coefficient is defined as the ratio of the correct quantity of a specific category to the total number of that category in the ground investigation. User's coefficient represents the ratio of the proper amount of a particular category to the total number of that category in the remotely sensed image. Producer's coefficient reflects correct classifications compared to reference data, while user's coefficient measures correctness against classification results.

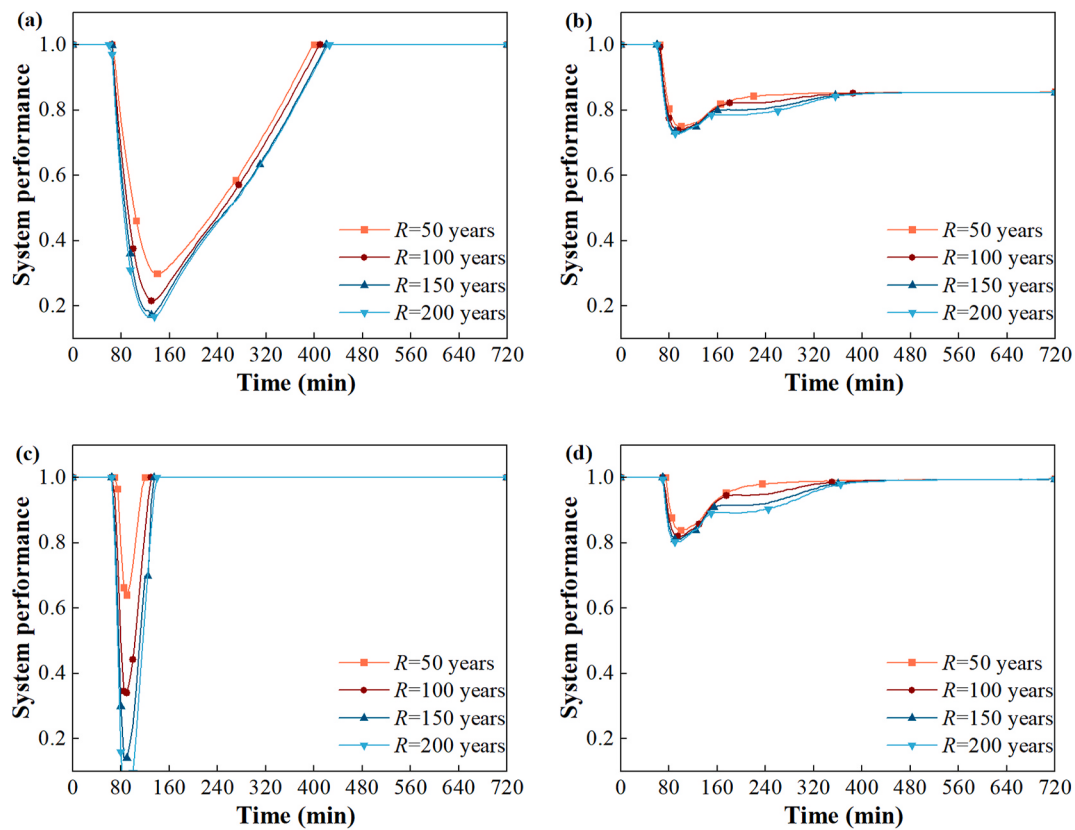


Fig. 5. Variation in system performance of representative grids (a) P1, (b) P2, (c) P3, and (d) P4 under four design rainfalls. All system performance curves initially decrease from 1, then gradually increase.

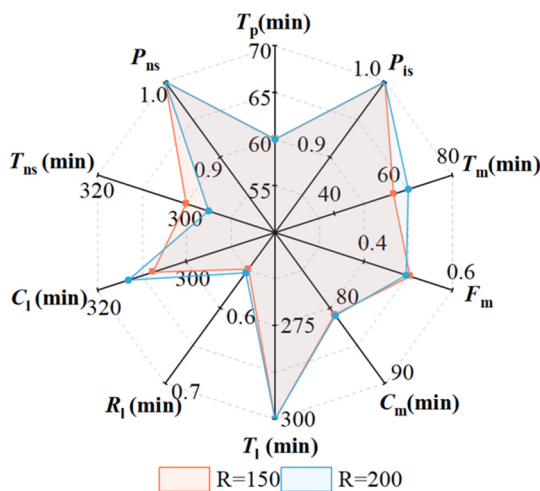


Fig. 6. Morphological feature parameters of grid P1 under multiple rainfall scenarios.

high and very high levels. In the design rainfall with a return period of 200 years, catchments with very low and low areas also appeared in Nanshahekou, Xi'anlu, Chunliu, and Xinghaiwan Subdistricts. However, the numbers showed a clear upward trend, with values of 5, 9, 2, and 5. Furthermore, the catchment areas with high levels of resilience progressively decreased from 1025 to 962 across the four design rainfall scenarios. In contrast, the percentage of catchment areas in forested areas increased with increasing return periods, reaching 16.7 %, 17.3 %, 17.6 %, and 17.8 %, respectively. The spatial pattern provides empirical evidence for the effectiveness of urban forests in enhancing resilience.

4.3. Resilience mechanisms

Identifying resilience mechanisms across similar urban flooding events equips stakeholders with a stronger basis for refining disaster response and mitigation strategies. The feature parameters of clusters were discussed using a 200-year return period scenario as a representative case (Fig. S4 and 8a). The accuracy of the cluster number determines the quality of the model. Considering both model fit and BIC result, the optimal choice for K was determined to be 4 (Fig. S8). Clusters 1 and 2 exhibited significant resilience capabilities, with values of 0.995 and 0.971, respectively. The F_m and R_l of the clusters were both approximately 0.9, in contrast to the lower values observed for clusters 3 and 4. Catchments in cluster 1 were the most numerous, accounting for 50 % of the total (Fig. S4). In contrast, clusters 3 and 4 experienced more severe urban flooding, which accounted for 17 % of the total and lacked adequate disaster response and recovery capacity. Two groups showed significant retardation and mediocrity in the dimensions of duration, the positions of the centroid, and the level of balance in the new phase. Clusters 3 and 4 were mainly located in lower-lying areas with denser road networks (Fig. S4). In particular, the system performance of the new stage (P_{ns}) was only 0.21 in cluster 3, indicating significant drainage problems in those catchment areas (Fig. 8a).

Urban form characteristics have a complex influence on urban flood resilience. Fig. 8b illustrates the interaction of the four distinct disaster response and recovery mechanisms with urban form characteristics under a 200-year return period scenario. Overall, the four mechanisms showed a complex correlation with the characteristic parameters of urban form. TA ($p < 0.05$), AS ($p < 0.05$), and AE ($p < 0.01$) for cluster 1 were positively correlated with urban flood resilience. PR ($p < 0.01$), TA ($p < 0.01$), and AE ($p < 0.01$) for cluster 2 were positively correlated with urban flood resilience, while RD ($p < 0.01$) was negatively correlated. These areas were characterized by their unique natural and

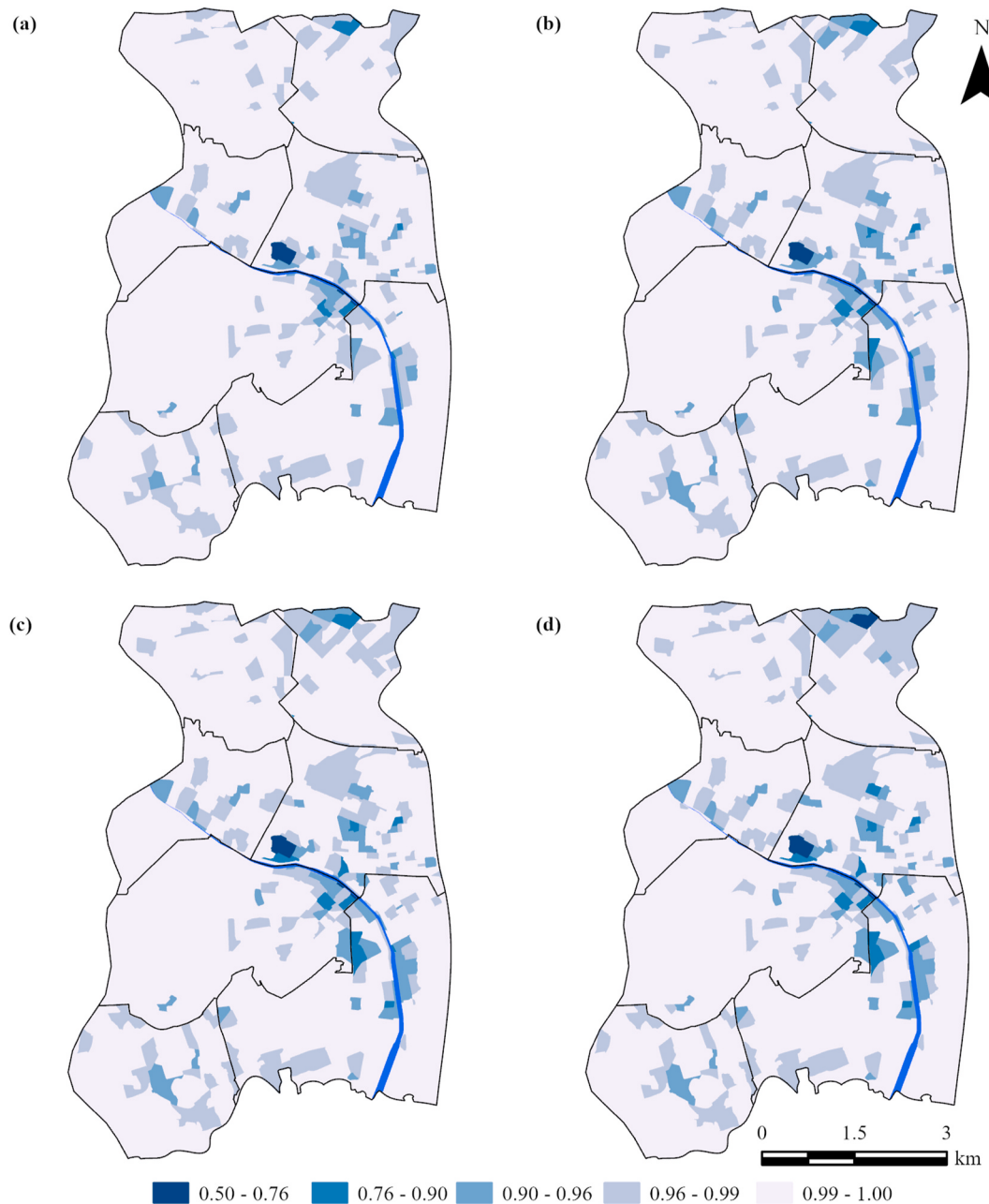


Fig. 7. Flood resilience maps for Shahekou under scenarios with return periods of (a) 50, (b) 100, (c) 150, and (d) 200 years. Darker colors indicate areas with lower resilience in the catchments. The resilience values of catchments are divided into five categories using the natural breakpoint method: 0.50–0.76 is very low, 0.76–0.90 is low, 0.90–0.96 is medium, 0.96–0.99 is high, and 0.99–1.00 is very high.

landscape conditions, marked by their distance from rivers and the diversity of their terrain. Cluster 1, in particular, had more elevated and slightly steeper terrain as well as more varied patches compared to cluster 2. In contrast, clusters 3 and 4 exhibited relatively weaker resilience. RD was negatively correlated with flood resilience ($p < 0.05$) in cluster 3, with a Pearson correlation coefficient of 0.41. It is indicated that the recovery rate and degree are not satisfactory due to larger landscape patches and poor drainage. SHDI ($p < 0.05$), PR ($p < 0.01$), TA ($p < 0.05$), and AE ($p < 0.05$) for cluster 4 were positively correlated with urban flood resilience, while RD ($p < 0.01$) was negatively correlated. Pearson correlation coefficients between flood resilience and PR, as well as between flood resilience and RD, showed moderate positive associations with values of 0.41 and 0.57, respectively. Results indicated that the catchments of cluster 4 were characterized by a high density of roads and a low landscape concentration, which contributed to a low

capacity for adaptation and recovery.

5. Discussion

5.1. Advantages of the proposed method

This study aims to quantitatively explore urban flood resilience by analyzing the morphological characteristics of the system performance curve. Compared with previous studies, the approach followed in this work has two distinct advantages in assessing resilience. First, typical flood depths and flow rates are simulated as system performance indicators rather than considering only flood depth. The design more comprehensively characterizes the intensity of the system. Second, this study develops a multi-stage quantification method that captures dynamic changes in resilience throughout the disaster timeline. As shown

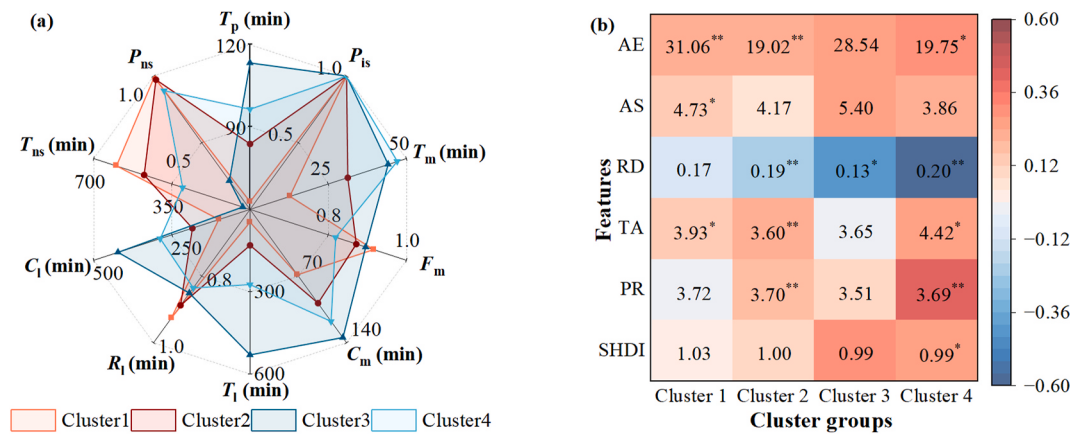


Fig. 8. Cluster analysis under a 200-year return period scenario. (a) Feature parameters for different clusters, and (b) pearson correlation between urban landscape characteristics include Average Elevation (AE), Average Slope (AS), Road Density (RD), Total Area (TA), Patch Richness (PR), and Shannon's Evenness Index (SHDI). The number represents the average values of urban form characteristics. “*” and “**” represent correlation coefficient significance at the 0.05 level and 0.01 level, respectively.

in Fig. 5 and S5, the combined effects of flood depth and flow velocity throughout the entire disaster process resulted in variable changes in system performance across different stages. Rapid socioeconomic development continuously improved flood preparedness capabilities, including improvements to the flood control system and the expansion of natural absorption areas. Before $t = 60$ min, the system performance remained stable at 1, indicating that the grids were in the early stage of urban flood resilience. When faced with torrential rain disasters, the urban drainage system is activated to minimize damage. Although flood depths and flow rates gradually developed, the intensity did not reach levels that would significantly impact critical infrastructure or daily life, so system performance remained stable. When the grid in the low-lying area exceeded the threshold for flood risk, the performance of the four grids began to decline approximately at $t = 60$ min. The grids then transitioned from the early stage to the middle stage. During such periods, the city utilizes its resources to rescue citizens, avoid permanent damage, and maintain essential services. At $t = 125, 90, 85$, and 90 min, the superposition of the flood and flow rates greatly affected P1, P2, P3, and P4, causing the system performance to reach a minimum. P1 and P2, which were both construction sites with densely crowded buildings, exhibited a moderating effect on flow velocity, which could potentially offer greater protection for residents and vehicles. Therefore, the grid maintained normal functionality throughout. Conversely, P3 and P4, located on roads with higher flow velocities, demonstrated different behaviors. The greater depth and flow velocity at P3 resulted in a longer duration for the dimensionless impact parameter to exceed the threshold. As flood intensity gradually recedes, government decisions begin to take effect, and the city slowly recovers. During the late phase, system performance recovers from its lowest point and eventually stabilizes at a new equilibrium. For example, at $t = 425$ min, P2 and P4 began to stabilize. The different nature of the land caused the P4 flow rate to slow down, allowing residents and vehicles to gradually return to stability. The results indicated a system performance value of 1 for P4, while that of P2 remained slightly below 1. The research results, therefore, provide a clear understanding of the overall performance and vulnerabilities at various stages of the disaster process.

Classic resilience methods primarily rely on the area under the system performance curve to represent resilience. However, two different systems may have identical areas under the curve during the middle or late stages, potentially misleading stakeholders in decision-making (Abbasnejadfar et al., 2022). As shown in Fig. S6, the resilience levels of subdistricts were calculated using both the classical and proposed methods. The results from the classical method tended to overestimate resilience. In particular, the catchments in the central part of the Xi'anlu Subdistrict had large centroidal values during the middle

and late stages, indicating that the areas had lower resilience. Due to varying interpretations of resilience, existing studies often apply inconsistent measurement criteria (Tang et al., 2023). The methods differ significantly and lead to different quantitative results. Methodological inconsistencies yield non-comparable quantitative results, complicating the synthesis of cross-study findings and their practical application. Overall, a resilience assessment method through the morphological characteristics of the performance curve may offer a more comprehensive evaluation of urban floods in a particular context.

5.2. Relationship between urban flood intensity and resilience

Flood intensity and flood resilience are often discussed together. Some researchers categorize the relationship between intensity and resilience into three main types: resilience capacity as a risk management objective, comprehensive risk-resilience capacity management, and resilience capacity as an alternative to risk management (Suter, 2012). In this study, urban flood resilience is considered a complement and refinement of flood risk management to address unexpected risks. An approach that separates risk from resilience will not only fail to find synergy but may also dissuade practitioners and scholars alike from leveraging existing risk-based approaches (Logan et al., 2022). Fig. 9 shows the relationship between flood intensity and resilience within each grid in the Shahekou District under a design rainfall with a return period of 200 years. The hexagon in the upper left corner is the reddest, indicating a predominant pattern of high resilience coupled with low intensity. The areas were mainly distributed in well-planned urban

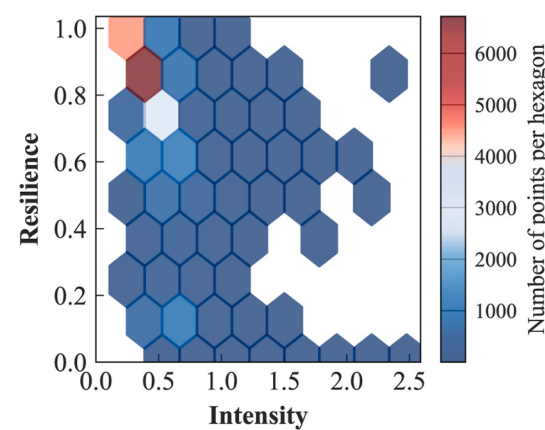


Fig. 9. Comparison of urban flood intensity and resilience for each grid.

spaces and densely vegetated forest areas. Soil infiltration and drainage infrastructure work together to mitigate surface runoff in the areas. Low-lying urban areas and extensive road networks exhibit an inverse relationship, demonstrating a pattern of high flood intensity and low resilience. This phenomenon is attributed to the combined effects of high surface imperviousness and the excessive load on drainage systems. The spatial distribution pattern offers valuable insights into urban flood control planning and resilience enhancement strategies. Moreover, there is a significant distinction between flood intensity and flood resilience. Flood intensity is determined by both occurrence probability and hazard characteristics, whereas resilience emphasizes the ability of a system to prepare for, withstand, recover from, and adapt to risks. Therefore, understanding the characteristics of flood intensity is a critical prerequisite for assessing flood resilience. Importantly, the relationship between flood intensity and resilience is not inherently oppositional. High flood intensity does not necessarily imply low resilience, and low intensity does not always correspond to high resilience. The figure also demonstrates that areas with low intensity have low resilience. For example, the hexagon that represents an intensity level of 0.5–1 and a resilience level of 0–0.2 contained more points than adjacent areas, indicating lower resilience within that intensity level. The flood resilience of grids with the same intensity level varies within a specific range, and intensity levels for grids with the same resilience also change within a limited range (Wang et al., 2023). This variation is primarily due to differences in land cover. When the intensity level is within the acceptable range of the grid, such as a green or forest field, the system can continue to maintain critical functions and operate smoothly. This gives rise to the possibility of high risk and high resilience. Conversely, low intensity may have a significant impact on the road, reflecting a scenario of low intensity and low resilience. An awareness of the complex relationship between flood intensity and resilience is crucial for developing effective risk management and enhancing adaptive capacity.

5.3. Spatial patterns of resilience across different clusters

Reasonable and differentiated urban planning is critical for enhancing flood resilience. This analysis reveals distinct spatial patterns of resilience across different clusters, underscoring the need for targeted interventions. First, cluster 3 exhibits the most severe flood impacts and the lowest system performance values. These regions are characterized by large landscape patches and inadequate drainage infrastructure, which collectively hinder effective recovery. In addressing these deficiencies, government interventions focus on enhancing landscape diversity, upgrading drainage systems to increase capacity, and constructing pumping stations to accelerate recovery. Second, cluster 4 areas are predominantly situated in low-lying regions adjacent to rivers. Improving landscape connectivity and creating multiple runoff pathways would complement existing structural flood defenses. This integrated strategy significantly enhances the adaptive capacity of the flood-prone areas. In contrast, clusters 1 and 2 demonstrate higher flood resilience due to the distal location from riverine systems. For these areas, investment in decentralized green infrastructure presents a cost-effective strategy for stormwater management. Additionally, forests exhibit high resilience (Fig. 7). Urban trees and forests reduce stormwater runoff through soil infiltration, canopy interception, and transpiration (Phillips et al., 2019). Tree selection for stormwater management focuses on interception and transpiration partitioning as they are the “first line of defense” (Rahman et al., 2023). In the future, mixed cultivation may be a viable solution, but the specific plan is carefully tailored to the local climate and conditions. Overall, by identifying the different needs of each area, urban planners allocate resources more efficiently and enhance resilience to withstand future urban flooding events.

5.4. The way forward

Despite its strengths, the present study has inherent limitations. First, the assumption of stationarity in extreme precipitation events may no longer be held under contemporary climatic and anthropogenic pressures. Precipitation patterns are becoming increasingly non-stationary and nonlinear, driven by global warming, land-use changes, and rapid urbanization (Zhang et al., 2023). Hence, it is imperative to update the design rainfall data for Dalian City to reflect the evolving hydrological conditions, ensuring more accurate flood assessments. Additionally, urban lakes play an essential flood-buffering role in temporal floodwater detention during flood seasons (Chen et al., 2022b). The lake system was not included in the study area. Subsequent studies ought to examine the mechanisms by which lake water bodies influence urban flood resilience and work toward developing a more comprehensive assessment model.

6. Conclusions

A novel flood resilience metric was proposed based on the morphological characteristics of the system performance curves. By assessing flood resilience under multiple disaster scenarios in Shahekou District, Dalian City, China, the study reaches the following main conclusions: Morphological parameters effectively capture resilience dynamics across different stages, especially the application of the centroid in the middle and late stages. While the two grids show similar characteristics, the positions of centroids differ significantly: 81.03 and 80.83 min in the middle stage and 313.07 and 307.53 min in the late stage. A negative correlation exists between rainfall intensity and system resilience, which tends to expand in areas with extremely low and low resilience under extreme scenarios. In a 50-year return period rainfall, areas with very low and low resilience were primarily concentrated in the low-altitude regions of Nanshahekou, Xi'anlu, Chunliu, and Xinghaiwan Subdistricts, with 4, 3, 2, and 1 catchments, respectively. In a 200-year return period scenario, the number of catchments increases to 5, 9, 2, and 5, respectively. Cluster analysis identified four distinct resilience patterns based on the morphology of the performance curve. While clusters 1 and 2 had significant resilience capacity, the other two clusters experienced more widespread damage and displayed retarding mechanisms in the middle and late stages. The correlations with road density were predominantly negative in clusters 3 and 4, with Pearson correlation coefficients of 0.41 and 0.57, respectively. The findings suggest future urban planning will prioritize interventions in clusters with the weakest resilience, particularly focusing on the construction of transportation infrastructure and green spaces.

CRediT authorship contribution statement

Mingyang Liu: Methodology, Investigation, Formal analysis, Conceptualization, Writing – original draft, Visualization, Software. **Ying Zhao:** Writing – review & editing, Supervision, Investigation. **Xiangzhou Xu:** Writing – review & editing, Supervision, Methodology, Funding acquisition, Conceptualization. **Hongwu Zhang:** Methodology, Writing – review & editing, Funding acquisition.

Declaration of competing interest

The authors declare that they have no known competing financial interests or personal relationships that could have appeared to influence the work reported in this paper.

Acknowledgments

This study was supported by the open competition project of 2024 major demonstration Engineering with science and technology innovation in the Inner Mongolia Autonomous Region, China (no. 2024JBGS0016) and National Natural Science Foundation of China (no.

52379060).

Appendix A. Supplementary data

Supplementary data to this article can be found online at <https://doi.org/10.1016/j.jenvman.2025.126691>.

Data availability

The authors do not have permission to share data.

References

- Abbasnejadfar, M., Bastami, M., Abbasnejadfar, M., Borzoo, S., 2022. Novel deterministic and probabilistic resilience assessment measures for engineering and infrastructure systems based on the economic impacts. *Int. J. Disaster Risk Reduct.* 75, 102956. <https://doi.org/10.1016/j.ijdr.2022.102956>.
- Ayyub, B.M., 2013. Systems resilience for multihazard environments: definition, metrics, and valuation for decision making. *Risk Anal.* 34 (2), 340–355. <https://doi.org/10.1111/risa.12093>.
- Chen, J., Chen, W., Huang, G., 2021. Assessing urban pluvial flood resilience based on a novel grid-based quantification method that considers human risk perceptions. *J. Hydrol.* 601, 126601. <https://doi.org/10.1016/j.jhydrol.2021.126601>.
- Chen, S., Zhang, Y., Lin, X., Lu, X., 2022a. Spatiotemporal characteristics analysis of water saving potential and economic effectiveness of rainwater harvesting system in China. *Water Supply* 22 (4), 4606–4623. <https://doi.org/10.2166/ws.2022.121>.
- Chen, T., Song, C., Zhan, P., Yao, J., Li, Y., Zhu, J., 2022b. Remote sensing estimation of the flood storage capacity of basin-scale lakes and reservoirs at high spatial and temporal resolutions. *Sci. Total Environ.* 807, 150772. <https://doi.org/10.1016/j.scitotenv.2021.150772>.
- Cheng, Y., Elsayed, E.A., Huang, Z., 2021. Systems resilience assessments: a review, framework and metrics. *Int. J. Prod. Res.* 60 (2), 595–622. <https://doi.org/10.1080/00207543.2021.1971789>.
- Debnath, J., Sahariah, D., Lahon, D., Nath, N., Chand, K., Meraj, G., Kumar, P., Kumar Singh, S., Kanga, S., Farooq, M., 2023. Assessing the impacts of current and future changes of the planforms of river Brahmaputra on its land use-land cover. *Geosci. Front.* 14 (4), 101557. <https://doi.org/10.1016/j.gsf.2023.101557>.
- Dong, B., Xia, J., Li, Q., Zhou, M., 2022. Risk assessment for people and vehicles in an extreme urban flood: case study of the “7.20” flood event in Zhengzhou, China. *Int. J. Disaster Risk Reduct.* 80, 103205. <https://doi.org/10.1016/j.ijdr.2022.103205>.
- Fan, C., Hou, J., Li, D., Chen, G., Guan, B., Wang, T., Pipin, L., Gao, X., 2024. Characteristics and drivers of flooding in recently built urban infrastructure during extreme rainfall. *Urban Clim.* 56, 102018. <https://doi.org/10.1016/j.ulclim.2024.102018>.
- Haghbin, S., Mahjouri, N., 2023. Quantifying and improving flood resilience of urban drainage systems based on socio-ecological criteria. *J. Environ. Manag.* 339, 117799. <https://doi.org/10.1016/j.jenvman.2023.117799>.
- Lazzarin, T., Viero, D.P., Molinari, D., Ballio, F., Defina, A., 2022. Flood damage functions based on a single physics- and data-based impact parameter that jointly accounts for water depth and velocity. *J. Hydrol.* 607, 127485. <https://doi.org/10.1016/j.jhydrol.2022.127485>.
- Liu, M., Wang, Q., Xu, X., Li, M., Wu, R., 2024a. Assessment of waterlogging resilience in Zhengzhou City considering waterlogging cycle. *Water Resour. Prot.* 40 (4), 48–55. <https://doi.org/10.3880/j.issn.10046933.2024.04.006>.
- Liu, M., Xu, X., Xiao, P., Cao, Y., 2024b. Advocating integration of human responses in the flood resilience framework for inland cities of northern China. *Water Policy* 26 (7), 652–670. <https://doi.org/10.2166/wp.2024.253>.
- Liu, Y., Han, J., Jiao, J., Liu, B., Ge, W., Pan, Q., Wang, F., 2022. Responses of flood peaks to land use and landscape patterns under extreme rainstorms in small catchments - a case study of the rainstorm of Typhoon Lekima in Shandong, China. *Int. Soil Water Conserv. Res.* 10 (2), 228–239. <https://doi.org/10.1016/j.iswcr.2021.07.005>.
- Logan, T.M., Aven, T., Guikema, S.D., Flage, R., 2022. Risk science offers an integrated approach to resilience. *Nat. Sustain.* 5 (9), 741–748. <https://doi.org/10.1038/s41893-022-00893-w>.
- McDermott, T.K.J., 2022. Global exposure to flood risk and poverty. *Nat. Commun.* 13 (1). <https://doi.org/10.1038/s41467-022-30725-6>.
- Mei, C., Shi, H., Liu, J., Song, T., Wang, J., Gao, X., Wang, H., Li, M., 2024. Analyzing urban form influence on pluvial flooding via numerical experiments using random slices of actual city data. *J. Hydrol.* 633, 130916. <https://doi.org/10.1016/j.jhydrol.2024.130916>.
- Nan, C., Sansavini, G., 2017. A quantitative method for assessing resilience of interdependent infrastructures. *Reliab. Eng. Syst. Saf.* 157, 35–53. <https://doi.org/10.1016/j.ress.2016.08.013>.
- Phillips, T.H., Baker, M.E., Lautar, K., Yesilomis, I., Pavao-Zuckerman, M.A., 2019. The capacity of urban forest patches to infiltrate stormwater is influenced by soil physical properties and soil moisture. *J. Environ. Manag.* 246, 11–18. <https://doi.org/10.1016/j.jenvman.2019.05.127>.
- Qian, J., Du, Y., Liang, F., Yi, J., Zhang, X., Jiang, J., Wang, N., Tu, W., Huang, S., Pei, T., Ma, T., 2024. Measuring community resilience inequality in inland flooding using location aware big data. *Cities* 149, 104915. <https://doi.org/10.1016/j.cities.2024.104915>.
- Rahman, M.A., Pawijit, Y., Xu, C., Pretsch, H., Rötzer, T., Pauleit, S., 2023. A comparative analysis of urban forests for storm-water management. *Sci. Rep.* 13 (1), 1–14. <https://doi.org/10.1038/s41598-023-28629-6>.
- Rentschler, J., Avner, P., Marconcini, M., Su, R., Strano, E., Voudoukas, M., Hallegatte, S., 2023. Global evidence of rapid urban growth in flood zones since 1985. *Nature* 622 (7981), 87–92. <https://doi.org/10.1038/s41586-023-06468-9>.
- Shukla, N., Das, A., Mazumder, T., 2025. Assessment of urban form resilience: a review of literature in the context of the Global South. *Environ. Dev. Sustain.* 27, 2863–2899. <https://doi.org/10.1007/s10668-023-04058-3>.
- Simonovic, S.P., Peck, A., 2022. Resilience to climate change-caused flooding—metro Vancouver case study. *River* 1 (1), 47–59. <https://doi.org/10.1002/rvr2.6>.
- Su, X., Wang, L., Li, L., Li, X., Wang, Y., Liu, Y., Hu, Q., 2023. Assessing watershed flood resilience based on a grid-scale system performance curve that considers double thresholds. *Sustainability* 16 (20), 9101. <https://doi.org/10.3390/su16209101>.
- Suter, M., 2012. *Resilience and Risk Management in Critical Infrastructure Protection Policy*. Center for Security Studies (CSS), ETH Zürich, Zürich.
- Tang, J., Han, S., Wang, J., He, B., Peng, J., 2023. A comparative analysis of performance-based resilience metrics via a quantitative-qualitative combined approach: are we measuring the same thing? *Int. J. Disaster Risk Sci.* 14 (5), 736–750. <https://doi.org/10.1007/s13753-023-00519-5>.
- UNISDR, 2009. 2009 UNISDR terminology on disaster risk reduction. <https://www.unisdr.org/publication/2009-unisdr-terminology-disaster-risk-reduction>. (Accessed 31 July 2024).
- Vojtek, M., Vojtečková, J., 2016. Flood hazard and flood risk assessment at the local spatial scale: a case study. *Geomat. Nat. Hazards Risk* 7 (6), 1973–1992. <https://doi.org/10.1080/19475705.2016.1166874>.
- Wang, Y., Meng, F., Liu, H., Zhang, C., Fu, G., 2019. Assessing catchment scale flood resilience of urban areas using a grid cell based metric. *Water Res.* 163, 114852. <https://doi.org/10.1016/j.watres.2019.114852>.
- Wang, Y., Zhang, C., Chen, A.S., Wang, G., Fu, G., 2023. Exploring the relationship between urban flood risk and resilience at a high-resolution grid cell scale. *Sci. Total Environ.* 893, 164852. <https://doi.org/10.1016/j.scitotenv.2023.164852>.
- Wang, Y., Zhang, P., Xie, Y., Chen, L., Cai, Y., 2024. Machine learning insights into the evolution of flood resilience: a synthesized framework study. *J. Hydrol.* 643, 131991. <https://doi.org/10.1016/j.jhydrol.2024.131991>.
- WMO, 2020. Climate change and water. <https://wmo.int/about-us/world-meteorologic-day/wmd-2020/climate-change-and-water#:~:text=Climate%20change%20is%20causing%20the%20hydrological%20cycle,are%20not%20evenly%20distributed%20around%20the%20world>. (Accessed 31 July 2024).
- Wu, Y., Yu, G., Shao, Q., 2022. Resilience benefit assessment for multi-scale urban flood control programs. *J. Hydrol.* 613, 128349. <https://doi.org/10.1016/j.jhydrol.2022.128349>.
- Yuan, X., 2022. Analysis on Waterlogging Removal and Waterlogging Elasticity of Urban Drainage under Changing Conditions. Dalian University of Technology. <https://doi.org/10.26991/d.cnki.gdlu.2022.002499>.
- Zhang, C., Gu, X., Ye, L., Xin, Q., Li, X., Zhang, H., 2023. Climate informed non-stationary modeling of extreme precipitation in China. *Water. Res. Manag.* 37 (9), 3319–3341. <https://doi.org/10.1007/s11269-023-03504-1>.
- Zhang, J., Wang, H., Huang, J., Wang, Y., Liu, G., 2023a. A study on dynamic simulation and improvement strategies of flood resilience for urban road system. *J. Environ. Manag.* 344, 11870. <https://doi.org/10.1016/j.jenvman.2023.11870>.
- Zhang, Q., Wu, Z., Zhang, H., Dalla Fontana, G., Tarolli, P., 2020. Identifying dominant factors of waterlogging events in metropolitan coastal cities: the case study of Guangzhou, China. *J. Environ. Manag.* 271, 110951. <https://doi.org/10.1016/j.jenvman.2020.110951>.
- Zhang, X., Mao, F., Gong, Z., Hannah, D.M., Cai, Y., Wu, J., 2023b. A disaster-damage-based framework for assessing urban resilience to intense rainfall-induced flooding. *Urban Clim.* 48, 101402. <https://doi.org/10.1016/j.ulclim.2022.101402>.
- Zheng, J., Huang, G., 2023. A novel grid cell-based urban flood resilience metric considering water velocity and duration of system performance being impacted. *J. Hydrol.* 617, 128911. <https://doi.org/10.1016/j.jhydrol.2022.128911>.
- Zheng, J., Li, J., Zeng, J., Huang, G., Chen, W., 2024. Application of a time-dependent performance-based resilience metric to establish the potential of coupled green-grey infrastructure in urban flood management. *Sustain. Cities Soc.* 112, 105608. <https://doi.org/10.1016/j.scs.2024.105608>.
- Zhou, Y., Wu, Z., Liang, Q., Xu, H., Wang, H., Xue, W., 2024. Threshold and real-time initiation mechanism of urban flood emergency response under combined disaster scenarios. *Sustain. Cities Soc.* 108, 105512. <https://doi.org/10.1016/j.scs.2024.105512>.
- Zou, J., Duan, C., Chen, B., Wang, H., 2024. Assessment of waterlogging resilience in Beijing based on quantification of economic losses under climate change. *Water Resour. Prot.* 40 (06), 85–94. <https://doi.org/10.3880/j.issn.10046933.2024.06.010>.